Carbon microspheres with tailored texture and surface chemistry as electrode materials for supercapacitors

Abdelhakim Elmouwahidi, Esther Bailón-García, Agustín F Pérez-Cadenas, Alain Celzard, Vanessa Fierro, Francisco Carrasco-Marín

Carbon microspheres with tailored texture and surface chemistry as electrode materials for supercapacitors

Abdelhakim Elmouwahidi[1], Esther Bailón-García[1], Agustín F. Pérez-Cadenas[1], Alain Celzard[2], Vanessa Fierro[2], Francisco Carrasco-Marín[1]*

[1]Research Group in Carbon Materials, Inorganic Chemistry Department, Faculty of Sciences, University of Granada, Campus Fuente Nueva s/n. 18071, Granada, Spain.

[2]Université de Lorraine, CNRS, IJL, F-88000 Epinal, France.

KEYWORDS: Carbon microsphere, CO_2 activation, Nitrogen doping, supercapacitor

ABSTRACT

N-doped carbon microspheres have been prepared by controlled sol-gel polymerization of resorcinol and formaldehyde. The pristine carbon microspheres were activated with CO_2 and the sample activated for 90 min possessed the highest BET area, 1520 m^2 g^{-1}. After N-doping with urea, a 4 wt % N content was reached and the microspheres still had a high BET area of 1350 m^2 g^{-1} with a porosity composed mostly of micropores (<2 nm) and a high packing density of 0.87 g cm^{-3}. These N-doped microspheres were used as electrodes of supercapacitors, which showed a remarkable specific capacitance of 235 F g^{-1} at a current density of 125 mAg^{-1} in 1 mol L^{-1} H2SO4 as electrolyte. This was due to pseudo-capacitance reactions produced by the presence of N-groups. Furthermore, these electrodes were able to retain 56.5 % of the capacitance using a current density of 7 A g^{-1} as well as to retain 100% of the capacitance after 12000 galvanostatic charge-discharge cycles at 1 A g^{-1}.

1. Introduction

Batteries offer a high energy density and will therefore continue to provide power for many electronic devices. However, although batteries are capable of achieving remarkable energy densities, the same cannot be said for their power density, i.e., their energy storage capacity is very high, but they are not able to deliver it in short times.[1] Batteries must work in a linear and more constant way; otherwise, their temperature may rise and thus reduce their lifespan. Consequently, in applications that require high power in short times, for example in electric engines, batteries have a disadvantage.[2]

It is at this point that supercapacitors should play a role in supporting batteries in many electric applications.[1,2] Indeed supercapacitors, unlike batteries, work like accumulators, delivering stored electrical energy almost instantaneously.[3] Moreover, the charging time of supercapacitors is very low (1 second) compared to batteries (3-5 min)[4] and the supercapacitor can be charged and discharged an almost unlimited number of times.[5] Supercapacitors are ideal devices when rapid charging is required to meet a short-term energy need, whereas batteries are chosen to provide long-term energy. Therefore, attempts to couple lithium-ion batteries and supercapacitors are more than encouraging.[6,7] From this perspective, supercapacitors are very interesting and are the subject of extensive research for their integration in electric cars.[8,9] This integration of supercapacitors would also bring other advantages: supercapacitors can help to significantly reduce the recharging times of electric cars and, given their ability to perform an almost infinite number of cycles, they can protect the batteries when the engine is turned on and off, thus increasing the lifetime of the batteries. This is the reason why they are already being applied to Start-Stop systems that are so popular in the automotive market to improve vehicle efficiency and reduce fuel consumption and emissions of combustion engines. Moreover, the

technology associated with supercapacitors would also have a positive impact on the amount of energy collected by regenerative braking systems. Due to their high energy capacity and short charging times, a supercapacitor provides higher energy savings and a better braking absorption performance.[1] These technological developments will contribute to increasing the autonomy of electric cars. Consequently, research on supercapacitors is being promoted by the automotive industry.[10]

During the last decade, several carbon-based materials have been used as supercapacitor electrodes because of their high specific surface area, high electronic conductivity, high chemical stability, and low cost.[11–13] The capacitance can be enhanced by the presence of heteroatoms in the carbon network, which is a promising way to improve their electrochemical performance.[14–16] Various heteroatoms have been used to introduce surface functional groups in the carbon materials such as nitrogen,[17–20] phosphorus[5,21] and oxygen[22,23]. It has been shown that nitrogen doping can enhance the carbon surface properties, namely surface polarity, electrical conductivity, and electron-donor affinity,[24,25] which could significantly influence its electrochemical behaviour.

Nitrogen-containing porous carbon materials have been prepared using different nitrogen precursors such as melamine[19] and urea,[26] which can modify the surface chemistry of the carbon after its synthesis.[19,26] Another strategy is to subject a naturally N-rich precursor to carbonization, such as melamine[27–29] or polyaniline, for the preparation of the nitrogen-enriched carbon materials[25,30,31] in a single-step process.

The electrochemical performance of the supercapacitor can be influenced not only by the presence of heteroatoms on the carbon surface but also by its pore size distribution and surface area.[32] Therefore, the presence of a large surface area with a hierarchical pore size distribution is

a crucial factor for a good capacitance. Different physical and chemical activation methods have been used to improve the textural properties of carbon materials such as chemical activation with KOH,[19,33] H_3PO_4,[5,34] $CaCl_2$ or $ZnCl_2$[35,36] or physical activation of the carbonized material with an oxidizing agent such as steam[37,38] or CO_2[38–40]. Activation of carbons under CO_2 flow is one of the most effective methods for the development of their textural properties.

In this study, we report the synthesis and the electrochemical behaviour of N-doped carbon microspheres with a highly developed surface area as electrodes of supercapacitors. For this purpose, microspheres were synthesized using a mixture of resorcinol and formaldehyde and submitted to carbonization. The as-obtained carbon microspheres were first activated with CO_2 and then functionalized with N-containing groups to improve their electrochemical performance. The effect of activation time on the surface area, pore size distribution and surface chemistry of the carbon microspheres was studied in-depth and related to the electrochemical performance of the corresponding supercapacitor electrodes.

2. Materials and methods

Materials

Resorcinol (99 %, Alfa Aesar), formaldehyde (37 %, Sigma-Aldrich), n-heptano (99.8 %, VWR), Span 80 (Sigma-Aldrich), Urea (99 %, Merck). Discs of 5 mm were cut from a graphite paper (240 μm, Sigma-Aldrich) and glass microfibre filters (pore size 1.6 μm) to be used as electrode and grassy fibrous separator, respectively.

Preparation of carbon microspheres

Carbon xerogel microspheres were prepared by inverse-emulsion sol-gel polymerization of resorcinol and formaldehyde in an organic medium. In a typical synthesis procedure, Span® 80 non-ionic surfactant (S) was dissolved in 900 mL of n-heptane and heated at 70 ºC under

reflux and stirring (450 rpm). A mixture containing resorcinol (R), formaldehyde (F) and water (W) was pre-gelled at 65 ºC for 1 h and then added dropwise into the above solution. The molar ratios of the mixture were R/F = 1/2, R/W = 1/14 and R/S = 4.5.

The gel microspheres were aged at 70 ºC for 24 h under stirring after which the suspension was filtered and the resulting filtrate was placed in acetone (5 days, changing acetone twice daily) to exchange water within the pores for acetone aiming to reduces the collapse of porosity during the subsequent drying process[41] and to remove the Span 80. Finally, the xerogel microspheres were dried by microwave heating under argon atmosphere (Ar flow is introduced by a hole input on the back of the microwave) in periods of 1 minute at 300 W until constant weight using a Saivod MS-287W microwave oven without temperature control, and then submitted to carbonization at 900 ºC for 2 h in a tubular furnace under a 300 cm^3 min^{-1} N_2 flow to obtain carbon xerogel microspheres. The final carbonization temperature was reached at a heating rate of 1 ºC min^{-1} in order to allow a gentle removal of pyrolysis gases.

The carbon xerogel microspheres (250 mg) were then activated at 900 ºC under CO_2 flow (60 cm^3 min^{-1}) for times ranging from 30 to 120 min. The activated samples were labelled as S-X, where X is the CO_2 activation time. For example, S-30 refers to carbon microspheres that were activated for 30 min.

The CO_2 activated carbon microspheres were functionalized with nitrogen groups by mixing the microspheres with urea in a mass ratio of 1:1 and were then subjected to thermal treatment at 350 ºC under air flow (300 cm^3/min) in a tubular furnace for 3 h. The nitrogen-doped samples were referred to as S-X-U, where U refers to the urea treatment. In order of comparison, a sample with prepared using more amount of urea (carbon:urea mass ratio of 1:2) was also synthesized (S-90-2U).

Textural and chemical characterization of carbon microspheres

The textural characterization of the carbon samples was carried out by adsorption of N_2 at -196 °C and CO_2 at 0 °C using an Autosorb-1 system and an ASAP 2020 equipment from Quatachrome and Micromeritics, respectively. The carbon samples were previously degassed at 120 ºC for 24 h under vacuum. The total micropore volume (W_0 (N_2)) and the average pore diameter ($L_0(N_2)$) and the BET area (A_{BET}) were determined by application of the Dubinin-Radushkevich (DR) equation and the BET method to the N_2 adsorption isotherms, respectively, and the volume (W_0 (CO_2)) and pore diameter ($L_0(CO_2)$) of narrow micropores were calculated using the DR equation applied to the CO_2 isotherms. The pore size distribution was determined by application of the Quenched Solid Density Functional Theory (QSDFT). The total pore volume ($V_{0.95}$) was considered as the volume of N_2 adsorbed at $P/P_0 = 0.95$. Mesopore volume V_{meso} was obtained as $V_{0.95}$-$W_0(N_2)$.

The chemical composition of activated carbons was obtained by elemental analysis using a CHNS elemental analyzer (ThermoFlash 1112) to determine carbon, hydrogen, nitrogen and sulfur contents by combustion of the samples in a stream of pure O_2. The oxygen content was determined by difference.

The surface chemistry of the carbon samples was characterized by X-ray photoelectron spectroscopy using an Escalab 200R system (VG Scientific Co.) equipped with a Mg Kα X-ray source (hν = 1253.6 eV) and hemispherical electron detector. For the analysis of the XPS peaks, the C1s peak position at 284.6 eV was used as a reference to locate the other peaks. The fitting of the XPS peaks was done by minimizing least squares using Gaussian-Lorentzian peak sharps and a Shirley's type background.

The morphology of the carbon microspheres was studied by scanning electron microscopy (SEM) and optical microscopy using a LEO (Carl Zeiss) GEMINI-1530 microscope and an OLYMPUS BX51 microscope, respectively. The images were analyzed with an appropriate software (IJ.JAR, from Java) to determine the mean diameter of carbon microspheres and the corresponding histograms. For this, a minimum of 1000 particles were analyzed from different microphotographs and their diameter was calculated assuming a perfect spherical shape.

Electrochemical characterization

Preparation of carbon electrodes

Electrodes were prepared as follows: a mixture of 90 % of carbon and 10 % of PTFE (60 % suspension in water) binder was prepared and dried overnight at 100 ºC. 5 mg of this dried mixture (containing 4.5 mg of active material) was pasted on a 5 mm graphite disc and pressed at 5 bars for a few minutes. Electrodes were impregnated with 1 mol L^{-1} H_2SO_4 for 48 h before being used for the electrochemical measurements.

Electrochemical measurements

The electrochemical measurements were carried out in an EC-lab system at 25 °C using a two-electrode system. 1 mol L^{-1} H_2SO_4 was used as electrolyte and a glassy fibrous material was used as separator. The electrochemical performance was analyzed in a voltage window of 0-0.9V. Cyclic voltammetry (CV) was performed at different scan rate (0.5, 2.5, 5, 10, 20 and 30 mV s^{-1}) and the gravimetric capacitance, C_{CV} (F g^{-1}), obtained as described elsewhere.[19,42] The galvanostatic charge-discharge tests were performed at current densities ranging from 0.125 to 7 A g^{-1} and the gravimetric capacitance, C_{GD} (F g^{-1}), was calculated as reported elsewhere.[43,44] The impedance spectroscopy measurements were carried out from 1 mHz to 100 kHz with AC amplitude of 10 mv. The electrical energies, E (Wh Kg^{-1}) and power densities, P(W Kg^{-1}) for

the two-electrode cell system were calculated as described elsewhere.[42,45] Cycling/Ageing experiments were performed at a current density of 1 A g^{-1} in the potential window between 0 and 0.9 V over 12000 charge–discharge cycles. More details were included in Supporting Information.

3. Results and Discussions

Morphology of the materials

The morphology of the pristine carbon microspheres was analyzed by optical and scanning electron microscopy, and representative images are shown in **Figure 1a,b** and **c,d**, respectively. It is clearly observed that carbon microspheres were successfully obtained by the inverse emulsion sol-gel polymerization of resorcinol and formaldehyde. These microspheres showed a perfect spherical morphology and a homogeneous size distribution with a mean size of 18 ± 3 μm (**Figure 1a,b** and **Figure S1**). Note also that, despite most of the carbon microspheres retained this spherical structure after carbonization (**Figure 1c**), some damaged microspheres were also observed, which allows their internal morphology to be observed (**Figure 1d**). A typical structure of carbon gels is observed inside the carbon microspheres, which consists of a reticulated network of interconnected nano-sized primary particles leaving a mesoporous structure between them. Besides, the fairly homogeneous size distribution of these microspheres is also important in terms of packing and electrolyte diffusion in order to make real and functional electrodes for supercapacitors. A high packing density of 0.87 g cm^{-3} was obtained.

Textural and chemical properties

N_2 adsorption-desorption isotherms of the CO_2-activated samples and their respective N-doped counterparts are depicted in **Figures 2a** and **2b**, respectively. Based on the IUPAC classification, all samples exhibit mixed type-I and type-IV isotherms, representative of micro

and mesoporous materials, respectively. The volume of N_2 adsorbed at low relative pressures increased with the activation time, indicating a predominantly micropore development during the CO_2 activation process. This increase is especially pronounced after 30 min of activation; however, activation times longer than 60 min increased N_2 adsorption but to a lesser extent. A similar tendency is observed for N-doped samples (**Figure 2b**). Nevertheless, lower N_2-adsorbed volumes are obtained at lower relative pressures than their respective CO_2-activated samples, indicating that the urea treatment reduced the surface area of the sample by blocking some porosity.[26]

The effect of the CO_2-activation time and the urea treatment on the porosity of carbon microspheres was analysed in more detail from the N_2 and CO_2 adsorption data included in **Table 1**. As previously commented, the CO_2-activation treatment of pristine carbon microspheres during 30 min caused an increase of surface area of 93 %, due to the opening of the existing ultra-microporosity and the creation of new, narrower, pores (the micropore volumes determined by N_2 and CO_2 adsorption, W_0 (N_2) and W_0 (CO_2), increased whereas the mesopore volume V_{meso} remained almost constant). It is well known that CO_2 adsorption provides information about the ultra-microporosity, i.e., micropores with a diameter narrower than 0.7 nm, while the super-microporosity is obtained from N_2 isotherm only in absence of diffusion restrictions. For pristine carbon microspheres (S-0), W_0 (N_2) < W_0 (CO_2), denoting the presence of narrow micropores or pores with constricted entrances, which prevent the access of N_2. However, W_0 (N_2) > W_0 (CO_2) for CO_2-activated samples, as a consequence of pore widening. Note that L_0 (N_2) also increased, corroborating this pore widening. Thus, the increase of activation time up to 90 min increased the surface area, average pore diameter and pore volume. However, the increase in activation time from 30 to 90 min caused an increase of surface area

substantially lower (18.9 %, from 30 to 60 min and 9.9 % from 60 to 90 min) compared to that observed from 0 to 30 min of activation (93 %). The surface area decreases for longer activation times such as 120 min probably due to pore widening and merging.[33] Thus, a maximum surface area was obtained after 90 min of CO_2 activation (**Figure 3a**). Hence, two antagonistic factors act together when the CO_2 activation time increases; one is the creation and opening of a porosity inaccessible to N_2 molecules and the other is the micropore widening and pore merging due to the disappearance of walls between adjacent pores. At low activation time, the first effect predominates and strongly increases the surface area, but by increasing the activation time the second effect starts to be important; it reduces the increase in surface area and even decreases the surface area at a very high activation time.

The micropore size distribution of CO_2-activated carbon microspheres is shown in **Figure 4a**. The micropore width of pristine microspheres (S-0) is very narrow and a well-defined peak is obtained at about 0.6 nm. Thus, some porosity could be inaccessible to N_2 molecules during adsorption at -196 °C. The intensity of this peak increased after 30 min of activation treatment (S-30), indicating the creation and opening of new ultra-microporosity, which highly increases the surface area. This intensity, as well as W_0 (N_2) (**Figure 3b**), slightly decreases while wider microporosity is created by increasing the activation time to more than 60 min (**Figure 4a**). This means that existing pores were destroyed or opened by excessively increasing the activating time due to the deterioration of the walls between adjacent micropores, which produced a reduction of surface area and micropore volume.

Regarding N-doped samples, the treatment with urea produced a decrease of the surface area compared to their respective CO_2-activated samples (**Table 1** and **Figure 3a**), due to a porosity blockage induced by the N-functionalization. However, the volumes of supermicropores

(0.7-2 nm, **Figure 4b**) and mesopores (**Table 1**) decreased after the urea treatment. From this, it can be concluded that N-functionalization mainly occurs in wider porosity without blocking the ultramicropores entrance and thus, N-surface groups are localized on a surface completely accessible for electrolyte ions and thus, for electrochemical reactions. Note that the volume of pores narrower than 0.7 nm, W_0 (CO_2), (**Table 1**), were not modified after the N-functionalization. Additionally, it is also important to highlight that the micropore width of the samples, L_0, which ranges from 0.62 to 1.27 nm, would be fully accessible to the hydronium ions, 0.36–0.42 nm,[34] and hydrated bisulphate ions, 0.53 nm,[35] produced by dissociation of the electrolyte (1 mol L^{-1} H_2SO_4).

The chemical nature of the bulk and surface of carbon materials was studied by elemental analysis and XPS, respectively, and results are collected in **Table 2**. From the results, it appears that CO_2 activation treatment did not affect the chemical nature of carbon spheres. All CO_2-activated samples, regardless to activation time, present a very low N (<0.5 %) and a constant oxygen (about 5.5 %) contents, which are very close to the values obtained for the pristine carbon spheres (S0). Thus, the different electrochemical behavior of CO_2-activated samples should only be related to their different textural characteristics since their chemical nature is quite similar. On the other hand, the treatment with urea highly increased the total N fixed on the carbon microspheres, whereas the O contents were not significantly modified. The amount of N fixed was around 4.0 ± 0.5 %, independently of the CO_2-activation time and therefore of the surface area and pore volume, except for the S-120-U sample in which the N content is slightly lower. Oxygen groups on carbon play a crucial role in the binding with nitrogen precursors, by providing active sites that promote the reaction with the N-doping molecules and N-integration in the carbon structure.[46–50] Mou *et al.*[46] found that certain oxygen-containing functional groups

in graphene oxide were responsible for reacting with the amino-groups of urea to form C–N bonds and allow N-doping. They therefore proposed that the process of formation of N-doped graphene starts with the reaction of amide and/or ammonia (produced by urea decomposition) with oxygen-containing functional groups in graphene sheets to form amidated graphene below ~300 °C. Then, amide N in amidated graphene is transformed to pyrrolic N and pyridinic N at the graphene edges and/or at defect sites between 300 and 500 °C. Here, the N % incorporated into the carbon network after the urea functionalization treatment of all CO_2-treated carbon microspheres (S-X-U series) is quite similar since the oxygen content of all CO_2-activated samples is almost the same. Even with twice the amount of urea (S-90-2U), the N content (3.9 %) was the same as that obtained when using a lower amount of urea (3.8 %). This fact seems to indicate that, in this study, the oxygen content was the limiting factor in the N-doping rather than the accessible surface area for urea functionalization.

Comparing the total and surface N contents, $N_{E.A.}$ and N_{XPS} respectively, it is observed that these two values are quite similar, indicating a homogeneous N distribution along the material surface. Conversely, $O_{E.A.}$ is much higher than O_{XPS}, indicating that most of this O is mainly a component of the carbon bulk structure. The nitrogen content will have an important effect on the electrochemical performance of the supercapacitors prepared.[27,51]

In order to obtain additional information about the nature of the N bonding, the N_{1s} spectral region was deconvolved for urea-treated carbon microspheres and the corresponding results are collected in **Table 2** and **Figure S2.** Three peaks are required for such deconvolution, which reveals the coexistence of three types of nitrogen: pyridinic-N (N-6) at 398.4 eV, pyrrolic-N or pyridone-N (N-5) at 400.1 eV, and quaternary nitrogen (N-Q) at 401.1 eV.[33,52,53] Note that N-6 and N-5 predominate (around 90 % of total N) in all urea-treated carbons. Moreover, this

distribution of N functionalities does not depend on the activation time of the carbon microspheres (**Table 2**). N-6 and N-5 functionalities could provide chemically active sites for pseudocapacitive reactions.[54] The electron-rich nature of these nitrogen sites indeed enhances the carbon basicity through a strong π delocalization in graphene layers and therefore, protons from the electrolyte can be attracted to the electrode surface and produce an enhancement in the capacitive behaviour in acidic electrolytes associated with the presence of these pseudocapacitive interactions.[33,55] N-Q can also increase the capacitance because graphene sheets with N-Q functionalities could be more positively charged when used as an anode material in supercapacitors, attracting more the ions charged negatively, thereby increasing the capacitance.

Alike nitrogen functional groups, oxygen functionalities also affect the capacitance of supercapacitors oxygen functionalities also affect the capacitance of supercapacitors. Therefore, O_{1s} spectral region was also deconvolved (**Table 2** and **Figure S2**)**.** In this case, two peaks are required for such deconvolution at 531 eV and 533 eV attributed to C=O and C-O bonds, respectively. However, note that O content and O-functionalities distribution is quite similar for all samples (N doped and undoped), consequently, the different electrochemical performed should be ascribed to the different textural properties and nitrogen functionalization.

Electrochemical properties

S-X-U samples combine a high surface area with a high nitrogen content and hence, the derived supercapacitors are expected to have a significant capacitive and cycling performance. **Figure 5a** and **b** show cyclic voltammograms (CVs) at 0.5 mV s^{-1} of the CO_2-activated carbon microspheres and their respective N-doped counterparts. It can be observed that CV curves of CO_2-activated samples have distorted rectangular shapes, whereas quasi-rectangular-shaped CV

curves were obtained for N-doped carbon microspheres. Moreover, the enclosed area of the CVs of N-doped samples is much higher than the one obtained for their respective CO_2-activated samples, despite their lower surface area and narrower pore width. This suggests a decrease in the internal resistance and an enhanced specific capacitance (**Table 3**) after nitrogen doping [56] that might be attributed to better ion transport, better wettability and higher electrical conductivity provided by the nitrogen functional groups. **Figure 6a** and **b** depicts the cyclic voltammograms at different scan rates for the sample S-90 and S-90-U, respectively. Note that the CV curves is deviated from the classical rectangular waveform, expected for a pure capacitor for the CO_2 treated sample (S-90), whereas this rectangular shape is maintained for N-doped sample (S-90-U) even at very high scan rate denoting the effect of the N-functional groups into the ion transport and the formation of the electrochemical double layer within the micropores. This fact was studied in more detail by analyzing the variation of the electrode capacitance as a function of scan rate (0.5–30 mV s^{-1}) displayed in **Figure 5c** and **d**. The specific electrode capacitance decreases as the scan rate increases because the formation of the electrochemical double layer (EDL) within the micropores is slower and less complete. At low scan rates, the electrolyte ions can easily diffuse and penetrate deeper into the material porosity, resulting in greater ion adsorption and therefore more effective interaction between the electrolyte and the electrode material and hence to a higher specific capacitance.[57] As the scan rate increases, the diffusion of electrolyte ions within the porous structure of the carbon becomes more difficult, and ineffective interactions between the electrolyte and electrode material occur, therefore the specific capacitance therefore decreases. Nonetheless, it should be noted that the decrease of the specific capacitance is more pronounced in CO_2-activated samples than in their respective N-doped counterparts, in spite of the porosity blockage and pore width narrowing observed after

functionalization. This clearly indicates that nitrogen surface groups favour capacitance retention. As commented, the electron-rich nature of N-6 and N-5 functional groups enhances the carbon basicity through a strong π delocalization in graphene layers and, therefore, the protons of the electrolyte can be attracted to the electrode surface, which promotes diffusion and adsorption of ions even at higher scan rates.

Galvanostatic charge–discharge tests were also performed and the results are shown in **Figure 7**. Similar conclusions can be obtained. The better capacitive behavior of N-doped samples regarding their CO_2-activated counterparts was also evidenced by their more triangular shape. It can be clearly seen that the charge/discharge curves of N-doped carbon microspheres are linear and symmetrical with low iR drops whereas asymmetrical curves with higher iR drops are observed for CO_2-activated samples, manifesting that the N-doping affects the current–voltage response and the electrochemical reversibility. The higher capacitance retention of N-doped samples is also pointed out in **Figure 7c** and **d**, indicating a lower electric resistance and a better diffusion of the electrolyte into the pore favored by the presence of N-surface groups.

The effect of the porous texture can be elucidated from **Figure 5a** and **7a** since, as it was pointed out in the previous section, CO_2-activated samples present a very similar surface chemistry. The enclosed area of the CVs and CPs for CO_2-activated samples increases in the sense S-0 < S-120 < S-30 ≈ S-60 < S-90. As expected, a very low electrode capacitance, C_{GD} and C_{CV} (**Table 3**), was obtained for the pristine carbon microspheres and this value increased with the activation time up to 90 min, due to the increase of available surface area for the development of the EDL. It is well known that the gravimetric capacitance increases with the micropore volume and surface area, indicating that both are key parameters for EDL formation on carbon-derived electrodes.[5,58] The specific capacitance decreased after 120 min of activation

due to the decrease in surface area and the pore widening observed at high activation time. A similar trend was obtained for N-functionalized samples; the higher the surface area and micropore volume, the higher the specific capacitance. Nonetheless, the capacitance proportionally increased for all activation times after N-doping, denoting that N-functionalization affects the capacitance in a similar extent for all activation times due to the similar N content of all samples. In conclusion, the sample S-90-U had the best electrochemical performance because it combines high surface area and optimum pore size distribution with nitrogen functionalities, resulting in a high electrode capacitance (228 F g^{-1} at 0.125 A g^{-1}). Moreover, as a consequence of its high packing density, the carbon microspheres (S-90-U) exhibit large volumetric capacitance (199 F g^{-1} at 0.125 A g^{-1}) which is very important to make real and functional electrodes for supercapacitors. This high volumetric capacitance is comparable or superior to most of the values reported in the literature (see **Table 4**).

The resistance to the diffusion of the electrolyte inside the carbon pores can be measured by electrochemical impedance spectroscopy, EIS. **Figure 8a** and **b** present the EIS spectra in the form of Nyquist plots for both CO_2-activated and N-doped carbon microspheres, respectively. The values of the equivalent series resistance (ESR) of all the samples are listed in **Table 5**. The ESR results in three resistances: the intrinsic resistance of the active material, the electrolyte resistance and the active material/current collector interface resistance. Since the same electrolyte, collectors, and technique were used to assemble the cell, the ESR can be related to the conductive properties of the activated carbon electrodes for comparison purposes. All samples present low ESR values, indicating a facile electron and ion transport/diffusion in the carbon porosity. However, the ESR values of the N-functionalized samples are typically the half of their respective CO_2-activated samples indicating, as it was previously commented, that

surface nitrogen groups favor the diffusion of ions and enhance the conductivity of carbon materials.

The interfacial charge transfer resistance, R_{CT}, caused by the electric double layer capacitance and Faradaic reactions was also calculated from the two intercepts of the semicircle with the real axis,[59] and the corresponding values are included in **Table 5**. R_{CT} values were lower for N-functionalized carbon microspheres than for their CO_2-activated counterparts. This indicates a faster charge transfer and a better accessibility of electrolyte ions into pores of the electrode materials due to the presence of N-surface groups. The R_{CT} values for S-60-U and S-90-U are the lowest, showing that ion transport is the easiest and fastest for those samples due to the combination of a good conductivity and a good ion diffusivity provided by the N-surface groups and the large and accessible porosity provided by CO_2-activation. It is also important to highlight that S-0 and S-0-U present the highest ESR and R_{ct} values of their respective series due to their narrowest pore size distributions, which make it difficult for the electrolyte to diffuse within the carbon porosity.

The relaxation time constant (τ), see **Table 5**, which is a quantitative measure of the time necessary for the total discharge of the supercapacitors,[39] can be obtained from the frequency, f_0, at the maximum of the curves of the imaginary part of the capacitance, by the equation $\tau = 1/(2 \times \pi f_0)$. Smaller values of τ were obtained for N-doped samples and specifically with S-30-U and S-90-U, which indicates a better supercapacitor response.

The cyclic stability of supercapacitors is one of the main factors that can hinder their practical application. For this reason, **Figure 9** shows the variation in the gravimetric electrode capacitance with the number of charge-discharge cycles at 1 A g^{-1} to assess the long-term

stability of electrodes. All samples exhibit good long-term stability. Nonetheless, N-doped samples exhibit virtually no loss of capacitance after 12000 cycles in comparison with the 95% of capacitance retention of their CO_2-activated counterparts (**Table 3**), suggesting an improved stability provided by the N-functionalization. Ragone plots obtained from galvanostatic discharge at different current densities are displayed in **Figure 10** and the maximum and minimum energies and power densities are listed in **Table 5**. Both the maximum energy density (E_{max}) and the maximum power density (P_{max}) increased with activation time up to 90 min, which was attributed to the pore structure developing better by increasing the activation time. This maximum energy is at least twice as high for N-doped samples as for their CO_2-activated counterparts, demonstrating the beneficial effect of N-surface groups in improving the wettability and the mobility of ions in the microporous network. The superior performance of the sample S-90-U is due to its more developed porosity associated with the presence of nitrogen surface groups.

4. Conclusion

Carbon microspheres having high surface areas and porosity were synthesized thanks to a simple CO_2 activation pre-treatment before N-doping. N-doped carbon microspheres, with remarkably high amounts of N functionalities, very well distributed throughout the entire carbon matrix, were prepared by mixing carbon microspheres with urea and subjecting them to a temperature of 350 °C in air. These special textural and chemical characteristics are highly desirable for high-performance supercapacitors, which in our best cases had electrode capacitances of 235 F g^{-1} combined with 100% cyclability after 12000 charge-discharge cycles. Besides, the fairly homogeneous size distribution of these microspheres is also important in

terms of packing and electrolyte diffusion in order to make real and functional electrodes for supercapacitors.

ASSOCIATED CONTENT

Supporting Information. The following files are available free of charge.

Figure S1. Particle size distribution of carbon microspheres obtained from the analysis of optical microscopy images.

Figure S2. XPS spectra of urea-treated carbon microspheres: N1s and O1s

AUTHOR INFORMATION

Corresponding Author

* Dr. Esther Bailón-García, email: estherbg@ugr.es

Author Contributions

The manuscript was written through contributions of all authors. All authors have given approval to the final version of the manuscript.

Funding Sources

Spanish Ministry of Science, Innovation and Universities (RTI2018-099224-B-I00)

Junta de Andalucía (P12-RNM-2892 and RNM172)

Generalitat Valenciana (APOSTD/2019/030)

ACKNOWLEDGMENT

This work was supported by Spanish Ministry of Science, Innovation and Universities - State Research Agency-_Project ref. RTI2018-099224-B-I00 and Junta de Andalucía (grant numbers

P12-RNM-2892, RNM172). E. Bailón-García is grateful to Generalitat Valenciana for her postdoctoral fellowship (APOSTD/2019/030). “Unidad de Excelencia Química Aplicada a Biomedicina y Medioambiente” of the University of Granada (UEQ - UGR) is gratefully acknowledged for the technical assistance.

REFERENCES

(1) Simon, P.; Gogotsi, Y.; Dunn, B. Where Do Batteries End and Supercapacitors Begin? *Sceince* **2014**, *343* (March), 1210–1212. https://doi.org/10.1126/science.1249625.

(2) Smith, T. A.; Mars, J. P.; Turner, G. A. Using Supercapacitors to Improve Battery Performance. In *2002 IEEE 33rd Annual IEEE Power Electronics Specialists Conference. Proceedings (Cat. No.02CH37289)*; 2002; Vol. 1, pp 124–128 vol.1. https://doi.org/10.1109/PSEC.2002.1023857.

(3) Luo, X.; Wang, J.; Dooner, M.; Clarke, J. Overview of Current Development in Electrical Energy Storage Technologies and the Application Potential in Power System Operation. *Appl. Energy* **2015**, *137*, 511–536. https://doi.org/10.1016/j.apenergy.2014.09.081.

(4) Miller, J. R.; A.F., B. Electrochemical Capacitors: Challenges and Opportunities for Real-World Applications. *Electrochem. Soc. Interface* **2008**, *17* (1), 53–57. https://doi.org/10.1007/978-3-319-72413-3_17.

(5) Elmouwahidi, A.; Bailón-García, E.; Pérez-Cadenas, A. F.; Maldonado-Hódar, F. J.; Carrasco-Marín, F. Activated Carbons from KOH and H3PO4-Activation of Olive Residues and Its Application as Supercapacitor Electrodes. *Electrochim. Acta* **2017**, *229*, 219–228. https://doi.org/10.1016/j.electacta.2017.01.152.

(6) Dubal, D. P.; Ayyad, O.; Ruiz, V.; Gómez-Romero, P. Hybrid Energy Storage: The Merging of Battery and Supercapacitor Chemistries. *Chem. Soc. Rev.* **2015**, *44* (7), 1777–1790. https://doi.org/10.1039/c4cs00266k.

(7) Lukatskaya, M. R.; Dunn, B.; Gogotsi, Y. Multidimensional Materials and Device Architectures for Future Hybrid Energy Storage. *Nat. Commun.* **2016**, *7*, 1–13. https://doi.org/10.1038/ncomms12647.

(8) Bisschoff, W. A.; Dobshanskyi, O.; Gouws, R. Integration of Battery and Super-Capacitor Banks into a Single-Power System for a Hybrid Electric Vehicle. *2016 2nd Int. Young Sci. Forum Appl. Phys. Eng. YSF 2016 - Forum Proc.* **2016**, No. October 2016, 10–13. https://doi.org/10.1109/YSF.2016.7753749.

(9) Embrandiri, M.; Isa, D.; Arehli, R. An Electric Vehicle Conversion Using Batteries and Ultracapacitors. *J. Asian Electr. Veh.* **2011**, *9* (2), 1521–1527. https://doi.org/10.4130/jaev.9.1521.

(10) Allègre, A. L.; Bouscayrol, A.; Trigui, R. Influence of Control Strategies on Battery/Supercapacitor Hybrid Energy Storage Systems for Traction Applications. *5th IEEE Veh. Power Propuls. Conf. VPPC '09* **2009**, 213–220. https://doi.org/10.1109/VPPC.2009.5289849.

(11) Frackowiak, E. Carbon Materials for Supercapacitor Application. *Phys. Chem. Chem. Phys.* **2007**, *9* (15), 1774–1785. https://doi.org/10.1039/b618139m.

(12) Zhou, W.; Zhou, K.; Jia, J. *Nanomaterials in Advanced Batteries and Supercapacitors*; 2016. https://doi.org/10.1007/978-3-319-26082-2.

(13) Li, M.; Xiao, H.; Zhang, T.; Li, Q.; Zhao, Y. Activated Carbon Fiber Derived from Sisal with Large Specific Surface Area for High-Performance Supercapacitors. *ACS Sustain. Chem. Eng.* **2019**, *7* (5), 4716–4723. https://doi.org/10.1021/acssuschemeng.8b04607.

(14) Liu, W.; Mei, J.; Liu, G.; Kou, Q.; Yi, T.; Xiao, S. Nitrogen-Doped Hierarchical Porous Carbon from Wheat Straw for Supercapacitors. *ACS Sustain. Chem. Eng.* **2018**, *6* (9), 11595–11605. https://doi.org/10.1021/acssuschemeng.8b01798.

(15) Lu, H.; Liu, S.; Zhang, Y.; Huang, Y.; Zhang, C.; Liu, T. Nitrogen-Doped Carbon Polyhedra Nanopapers: An Advanced Binder-Free Electrode for High-Performance Supercapacitors. *ACS Sustain. Chem. Eng.* **2019**, *7* (5), 5240–5248. https://doi.org/10.1021/acssuschemeng.8b06159.

(16) Yan, L.; Li, D.; Yan, T.; Chen, G.; Shi, L.; An, Z.; Zhang, D. N,P,S-Codoped Hierarchically Porous Carbon Spheres with Well-Balanced Gravimetric/Volumetric Capacitance for Supercapacitors. *ACS Sustain. Chem. Eng.* **2018**, *6* (4), 5265–5272. https://doi.org/10.1021/acssuschemeng.7b04922.

(17) Vivo-Vilches, J. F.; Bailón-García, E.; Pérez-Cadenas, A. F.; Carrasco-Marín, F.; Maldonado-Hódar, F. J. Tailoring the Surface Chemistry and Porosity of Activated Carbons: Evidence of Reorganization and Mobility of Oxygenated Surface Groups. *Carbon N. Y.* **2014**, *68*, 520–530. https://doi.org/10.1016/j.carbon.2013.11.030.

(18) Kim, S. M.; Heo, Y. K.; Bae, K. T.; Oh, Y. T.; Lee, M. H.; Lee, S. Y. In Situ Formation of Nitrogen-Doped Onion-like Carbon as Catalyst Support for Enhanced Oxygen Reduction Activity and Durability. *Carbon N. Y.* **2016**, *101*, 420–430. https://doi.org/10.1016/j.carbon.2016.02.022.

(19) Elmouwahidi, A.; Zapata-Benabithe, Z.; Carrasco-Marín, F.; Moreno-Castilla, C. Activated Carbons from KOH-Activation of Argan (Argania Spinosa) Seed Shells as Supercapacitor Electrodes. *Bioresour. Technol.* **2012**, *111*, 185–190. https://doi.org/10.1016/j.biortech.2012.02.010.

(20) Hulicova-Jurcakova, D.; Seredych, M.; Lu, G. Q.; Bandosz, T. J. Combined Effect of Nitrogen- and Oxygen-Containing Functional Groups of Microporous Activated Carbon on Its Electrochemical Performance in Supercapacitors. *Adv. Funct. Mater.* **2009**, *19* (3), 438–447. https://doi.org/10.1002/adfm.200801236.

(21) Fan, X.; Yu, C.; Ling, Z.; Yang, J.; Qiu, J. Hydrothermal Synthesis of Phosphate-Functionalized Carbon Nanotube-Containing Carbon Composites for Supercapacitors with Highly Stable Performance. *ACS Appl. Mater. Interfaces* **2013**, *5* (6), 2104–2110. https://doi.org/10.1021/am303052n.

(22) Zhao, Y.; Ran, W.; He, J.; Song, Y.; Zhang, C.; Xiong, D. B.; Gao, F.; Wu, J.; Xia, Y. Oxygen-Rich Hierarchical Porous Carbon Derived from Artemia Cyst Shells with Superior Electrochemical Performance. *ACS Appl. Mater. Interfaces* **2015**, *7* (2), 1132–1139. https://doi.org/10.1021/am506815f.

(23) Calvo, E. G.; Rey-Raap, N.; Arenillas, A.; Menéndez, J. A. The Effect of the Carbon Surface Chemistry and Electrolyte PH on the Energy Storage of Supercapacitors. *RSC Adv.* **2014**, *4* (61), 32398–32404. https://doi.org/10.1039/c4ra04430d.

(24) Lahaye, J.; Nansé, G.; Bagreev, A.; Strelko, V. Porous Structure and Surface Chemistry of Nitrogen Containing Carbons from Polymers. *Carbon N. Y.* **1999**, *37* (4), 585–590.

https://doi.org/10.1016/S0008-6223(98)00225-5.

(25) Yan, J.; Wei, T.; Qiao, W.; Fan, Z.; Zhang, L.; Li, T.; Zhao, Q. A High-Performance Carbon Derived from Polyaniline for Supercapacitors. *Electrochem. commun.* **2010**, *12* (10), 1279–1282. https://doi.org/10.1016/j.elecom.2010.06.037.

(26) Zhao, W.; Fierro, V.; Fernández-Huerta, N.; Izquierdo, M. T.; Celzard, A. Hydrogen Uptake of High Surface Area-Activated Carbons Doped with Nitrogen. *Int. J. Hydrogen Energy* **2013**, *38* (25), 10453–10460. https://doi.org/10.1016/j.ijhydene.2013.06.048.

(27) Wang, Y.; Xuan, H.; Lin, G.; Wang, F.; Chen, Z.; Dong, X. A Melamine-Assisted Chemical Blowing Synthesis of N-Doped Activated Carbon Sheets for Supercapacitor Application. *J. Power Sources* **2016**, *319*, 262–270. https://doi.org/10.1016/j.jpowsour.2016.04.069.

(28) Friedel, B.; Greulich-Weber, S. Preparation of Monodisperse, Submicrometer Carbon Spheres by Pyrolysis of Melamine-Formaldehyde Resin. *Small* **2006**, *2* (7), 859–863. https://doi.org/10.1002/smll.200500516.

(29) Pérez-Cadenas, M.; Moreno-Castilla, C.; Carrasco-Marín, F.; Pérez-Cadenas, A. F. Surface Chemistry, Porous Texture, and Morphology of N-Doped Carbon Xerogels. *Langmuir* **2009**, *25* (1), 466–470. https://doi.org/10.1021/la8027786.

(30) Zhu, H.; Yin, J.; Wang, X.; Wang, H.; Yang, X. Microorganism-Derived Heteroatom-Doped Carbon Materials for Oxygen Reduction and Supercapacitors. *Adv. Funct. Mater.* **2013**, *23* (10), 1305–1312. https://doi.org/10.1002/adfm.201201643.

(31) Schur, F. Neue Begr??Ndung Der Theorie Der Endlichen Transformationsgruppen. *Math. Ann.* **1889**, *35* (1–2), 161–197. https://doi.org/10.1016/j.carbon.2015.03.038.

(32) Eftekhari, A. Surface Diffusion and Adsorption in Supercapacitors. *ACS Sustain. Chem. Eng.* **2019**, *7* (4), 3692–3701. https://doi.org/10.1021/acssuschemeng.8b01075.

(33) Zapata-Benabithe, Z.; Carrasco-Marín, F.; Moreno-Castilla, C. Preparation, Surface Characteristics, and Electrochemical Double-Layer Capacitance of KOH-Activated Carbon Aerogels and Their O- and N-Doped Derivatives. *J. Power Sources* **2012**, *219*, 80–88. https://doi.org/10.1016/j.jpowsour.2012.07.036.

(34) Li, Y.; Zhang, X.; Yang, R.; Li, G.; Hu, C. The Role of H3PO4 in the Preparation of Activated Carbon from NaOH-Treated Rice Husk Residue. *RSC Adv.* **2015**, *5* (41), 32626–32636. https://doi.org/10.1039/c5ra04634c.

(35) Caturla, F.; Molina-Sabio, M.; Rodríguez-Reinoso, F. Preparation of Activated Carbon by Chemical Activation with ZnCl2. *Carbon N. Y.* **1991**, *29* (7), 999–1007. https://doi.org/https://doi.org/10.1016/0008-6223(91)90179-M.

(36) Vargas, D. P.; Giraldo, L.; Moreno-Piraján, J. C. Characterisation of Granular Activated Carbon Prepared by Activation with CaCl2 by Means of Gas Adsorption and Immersion Calorimetry. *Adsorption* **2016**, *22* (4–6), 717–723. https://doi.org/10.1007/s10450-016-9764-2.

(37) Prakash Kumar, B. G.; Shivakamy, K.; Miranda, L. R.; Velan, M. Preparation of Steam Activated Carbon from Rubberwood Sawdust (Hevea Brasiliensis) and Its Adsorption Kinetics. *J. Hazard. Mater.* **2006**, *136* (3), 922–929. https://doi.org/10.1016/j.jhazmat.2006.01.037.

(38) Rodríguez-Reinoso, F.; Molina-Sabio, M.; González, M. T. The Use of Steam and CO2 as Activating Agents in the Preparation of Activated Carbons. *Carbon N. Y.* **1995**, *33* (1), 15–23. https://doi.org/10.1016/0008-6223(94)00100-E.

(39) Zhang, T.; Walawender, W. P.; Fan, L. T.; Fan, M.; Daugaard, D.; Brown, R. C. Preparation of Activated Carbon from Forest and Agricultural Residues through CO2 Activation. *Chem. Eng. J.* **2004**, *105* (1–2), 53–59. https://doi.org/10.1016/j.cej.2004.06.011.

(40) Moreno-Castilla, C.; Carrasco-Marín, F.; López-Ramón, M. V.; Alvarez-Merino, M. A. Chemical and Physical Activation of Olive-Mill Waste Water to Produce Activated Carbons. *Carbon N. Y.* **2001**, *39* (9), 1415–1420. https://doi.org/10.1016/S0008-6223(00)00268-2.

(41) Gallegos-Suárez, E.; Pérez-Cadenas, A. F.; Maldonado-Hódar, F. J.; Carrasco-Marín, F. On the Micro- and Mesoporosity of Carbon Aerogels and Xerogels. The Role of the Drying Conditions during the Synthesis Processes. *Chem. Eng. J.* **2012**, *181–182*, 851–855. https://doi.org/10.1016/j.cej.2011.12.002.

(42) Moreno-Castilla, C.; García-Rosero, H.; Carrasco-Marín, F. Symmetric Supercapacitor Electrodes from KOH Activation of Pristine, Carbonized, and Hydrothermally Treated Melia Azedarach Stones. *Materials (Basel).* **2017**, *10* (7). https://doi.org/10.3390/ma10070747.

(43) Zapata-Benabithe, Z.; Carrasco-Marín, F.; Moreno-Castilla, C. Electrochemical Performance of Cu- and Ag-Doped Carbon Aerogels. *Mater. Chem. Phys.* **2013**, *138* (2–3), 870–876. https://doi.org/10.1016/j.matchemphys.2012.12.076.

(44) Zapata-Benabithe, Z.; Carrasco-Marín, F.; De Vicente, J.; Moreno-Castilla, C. Carbon Xerogel Microspheres and Monoliths from Resorcinol-Formaldehyde Mixtures with Varying Dilution Ratios: Preparation, Surface Characteristics, and Electrochemical Double-Layer Capacitances. *Langmuir* **2013**, *29* (20), 6166–6173. https://doi.org/10.1021/la4007422.

(45) Korenblit, Y.; Rose, M.; Kockrick, E.; Borchardt, L.; Kvit, A.; Kaskel, S.; Yushin, G. High-Rate Electrochemical Capacitors Based on Ordered Mesoporous Silicon Carbide-Derived Carbon. *ACS Nano* **2010**, *4* (3), 1337–1344. https://doi.org/10.1021/nn901825y.

(46) Mou, Z.; Chen, X.; Du, Y.; Wang, X.; Yang, P.; Wang, S. Forming Mechanism of Nitrogen Doped Graphene Prepared by Thermal Solid-State Reaction of Graphite Oxide and Urea. *Appl. Surf. Sci.* **2011**, *258* (5), 1704–1710. https://doi.org/10.1016/j.apsusc.2011.10.019.

(47) Huang, Z.; Liao, Z.; Yang, W.; Zhou, H.; Fu, C.; Gong, Y.; Chen, L.; Kuang, Y. Different Types of Nitrogen Species in Nitrogen-Doped Carbon Material: The Formation Mechanism and Catalytic Role on Oxygen Reduction Reaction. *Electrochim. Acta* **2017**, *245*, 957–966. https://doi.org/10.1016/j.electacta.2017.06.026.

(48) Li, X.; Wang, H.; Robinson, J. T.; Sanchez, H.; Diankov, G.; Dai, H. Simultaneous Nitrogen Doping and Reduction of Graphene Oxide. *J. Am. Chem. Soc.* **2009**, *131* (43), 15939–15944. https://doi.org/10.1021/ja907098f.

(49) Sheng, Z. H.; Shao, L.; Chen, J. J.; Bao, W. J.; Wang, F. Bin; Xia, X. H. Catalyst-Free Synthesis of Nitrogen-Doped Graphene via Thermal Annealing Graphite Oxide with Melamine and Its Excellent Electrocatalysis. *ACS Nano* **2011**, *5* (6), 4350–4358.

https://doi.org/10.1021/nn103584t.

(50) Li, D.; Duan, X.; Sun, H.; Kang, J.; Zhang, H.; Tade, M. O.; Wang, S. Facile Synthesis of Nitrogen-Doped Graphene via Low-Temperature Pyrolysis: The Effects of Precursors and Annealing Ambience on Metal-Free Catalytic Oxidation. *Carbon N. Y.* **2017**, *115*, 649–658. https://doi.org/10.1016/j.carbon.2017.01.058.

(51) Wickramaratne, N. P.; Xu, J.; Wang, M.; Zhu, L.; Dai, L.; Jaroniec, M. Nitrogen Enriched Porous Carbon Spheres: Attractive Materials for Supercapacitor Electrodes and CO2 Adsorption. *Chem. Mater.* **2014**, *26* (9), 2820–2828. https://doi.org/10.1021/cm5001895.

(52) Gorgulho, H. F.; Gonçalves, F.; Pereira, M. F. R.; Figueiredo, J. L. Synthesis and Characterization of Nitrogen-Doped Carbon Xerogels. *Carbon N. Y.* **2009**, *47* (8), 2032–2039. https://doi.org/10.1016/j.carbon.2009.03.050.

(53) Kiciński, W.; Norek, M.; Jankiewicz, B. J. Heterogeneous Carbon Gels: N-Doped Carbon Xerogels from Resorcinol and n-Containing Heterocyclic Aldehydes. *Langmuir* **2014**, *30* (47), 14276–14285. https://doi.org/10.1021/la503207t.

(54) Wang, S.; Zhang, J.; Shang, P.; Li, Y.; Chen, Z.; Xu, Q. N-Doped Carbon Spheres with Hierarchical Micropore-Nanosheet Networks for High Performance Supercapacitors. *Chem. Commun.* **2014**, *50* (81), 12091–12094. https://doi.org/10.1039/c4cc04832f.

(55) Hulicova, D.; Kodama, M.; Hatori, H. Electrochemical Performance of Nitrogen-Enriched Carbons in Aqueous and Non-Aqueous Supercapacitors. *Chem. Mater.* **2006**, *18* (9), 2318–2326. https://doi.org/10.1021/cm060146i.

(56) Elessawy, N. A.; El Nady, J.; Wazeer, W.; Kashyout, A. B. Development of High-Performance Supercapacitor Based on a Novel Controllable Green Synthesis for 3D Nitrogen Doped Graphene. *Sci. Rep.* **2019**, *9* (1), 1–10. https://doi.org/10.1038/s41598-018-37369-x.

(57) Ali, G. A. M.; Tan, L. L.; Jose, R.; Yusoff, M. M.; Chong, K. F. Electrochemical Performance Studies of MnO2 Nanoflowers Recovered from Spent Battery. *Mater. Res. Bull.* **2014**, *60*, 5–9. https://doi.org/10.1016/j.materresbull.2014.08.008.

(58) Zapata-Benabithe, Z.; Moreno-Castilla, C.; Carrasco-Marín, F. Effect of Dilution Ratio and Drying Method of Resorcinol – Formaldehyde Carbon Gels on Their

Electrocapacitive Properties in Aqueous and Non-Aqueous Electrolytes. *J. Sol-Gel Sci. Technol.* **2015**, *75*, 407–412. https://doi.org/10.1007/s10971-015-3713-5.

(59) Elmouwahidi, A.; Castelo-Quibén, J.; Vivo-Vilches, J. F.; Pérez-Cadenas, A. F.; Maldonado-Hódar, F. J.; Carrasco-Marín, F. Activated Carbons from Agricultural Waste Solvothermally Doped with Sulphur as Electrodes for Supercapacitors. *Chem. Eng. J.* **2018**, *334* (November 2017), 1835–1841. https://doi.org/10.1016/j.cej.2017.11.141.

(60) Feng, S.; Liu, Z.; Yu, Q.; Zhuang, Z.; Chen, Q.; Fu, S.; Zhou, L.; Mai, L. Monodisperse Carbon Sphere-Constructed Pomegranate-Like Structures for High-Volumetric-Capacitance Supercapacitors. *ACS Appl. Mater. Interfaces* **2019**, *11* (4), 4011–4016. https://doi.org/10.1021/acsami.8b19901.

(61) Demir, M.; Saraswat, S. K.; Gupta, R. B. Hierarchical Nitrogen-Doped Porous Carbon Derived from Lecithin for High-Performance Supercapacitors. *RSC Adv.* **2017**, *7* (67), 42430–42442. https://doi.org/10.1039/c7ra07984b.

(62) Zhao, J.; Li, Y.; Wang, G.; Wei, T.; Liu, Z.; Cheng, K.; Ye, K.; Zhu, K.; Cao, D.; Fan, Z. Enabling High-Volumetric-Energy-Density Supercapacitors: Designing Open, Low-Tortuosity Heteroatom-Doped Porous Carbon-Tube Bundle Electrodes. *J. Mater. Chem. A* **2017**, *5* (44), 23085–23093. https://doi.org/10.1039/c7ta07010a.

(63) Han, J.; Li, Q.; Wang, J.; Ye, J.; Fu, G.; Zhai, L.; Zhu, Y. Heteroatoms (O, N)-Doped Porous Carbon Derived from Bamboo Shoots Shells for High Performance Supercapacitors. *J. Mater. Sci. Mater. Electron.* **2018**, *29* (24), 20991–21001. https://doi.org/10.1007/s10854-018-0244-1.

(64) Li, H.; Li, J.; Thomas, A.; Liao, Y. Ultra-High Surface Area Nitrogen-Doped Carbon Aerogels Derived From a Schiff-Base Porous Organic Polymer Aerogel for CO2 Storage and Supercapacitors. *Adv. Funct. Mater.* **2019**, *29* (40), 1904785. https://doi.org/10.1002/adfm.201904785.

(65) Ruiz-Rosas, R.; Valero-Romero, M. J.; Salinas-Torres, D.; Rodríguez-Mirasol, J.; Cordero, T.; Morallón, E.; Cazorla-Amorós, D. Electrochemical Performance of Hierarchical Porous Carbon Materials Obtained from the Infiltration of Lignin into Zeolite Templates. *ChemSusChem* **2014**, *7* (5), 1458–1467.

https://doi.org/10.1002/cssc.201301408.

(66) Chmiola, J.; Largeot, C.; Taberna, P. L.; Simon, P.; Gogotsi, Y. Monolithic Carbide-Derived Carbon Films for Micro-Supercapacitors. *Science (80-.).* **2010**, *328* (April), 480–484.

(67) Lei, Z.; Lu, L.; Zhao, X. S. The Electrocapacitive Properties of Graphene Oxide Reduced by Urea. *Energy Environ. Sci.* **2012**, *5* (4), 6391–6399. https://doi.org/10.1039/c1ee02478g.

(68) Ferrero, G. A.; Fuertes, A. B.; Sevilla, M. N-Doped Microporous Carbon Microspheres for High Volumetric Performance Supercapacitors. *Electrochim. Acta* **2015**, *168*, 320–329. https://doi.org/10.1016/j.electacta.2015.04.052.

(69) Rufford, T. E.; Hulicova-Jurcakova, D.; Fiset, E.; Zhu, Z.; Lu, G. Q. Double-Layer Capacitance of Waste Coffee Ground Activated Carbons in an Organic Electrolyte. *Electrochem. commun.* **2009**, *11* (5), 974–977. https://doi.org/10.1016/j.elecom.2009.02.038.

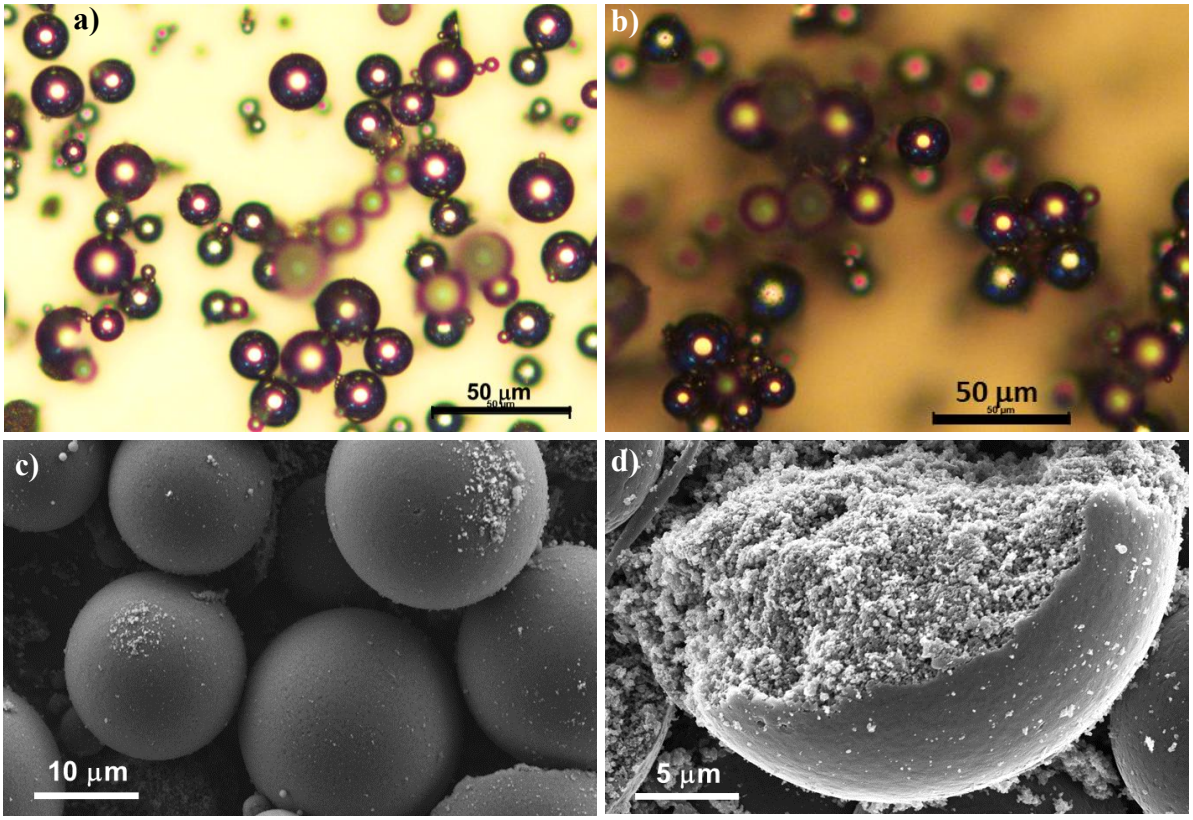

Figure 1. Optical (a and b) and SEM (c and d) images of pristine carbon microspheres.

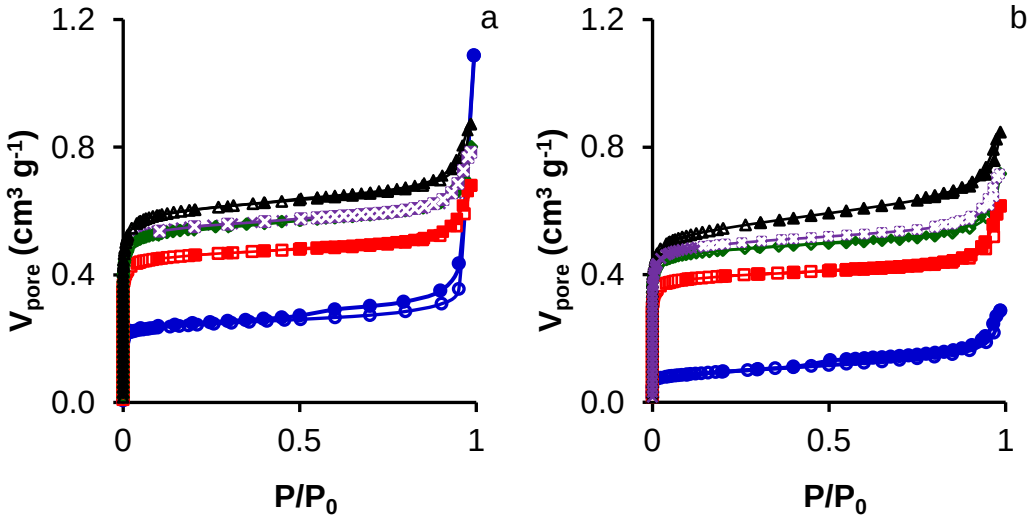

Figure 2. N_2 isotherms at -196 °C of (a) CO_2-activated carbon microspheres and (b) N-doped carbon microspheres. Samples: S-0 and S-0-U (○), S-30 and S-30-U (□), S-60 and S-60-U (◇), S-90 and S-90-U (△), S-120 and S-120-U (×). Open symbols, adsorption; closed symbols, desorption

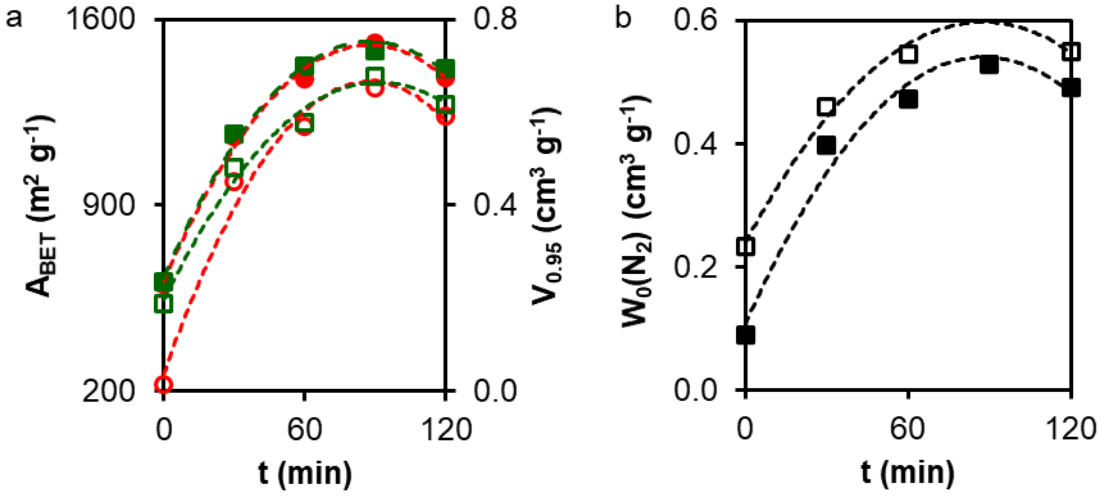

Figure 3. Variation of A_{BET} (○) and $V_{0.95}$ (□) (a), and W_0 (N_2) (b) as a function of activation time. Open symbol: non-doped, closed symbols: N-doped carbon microspheres.

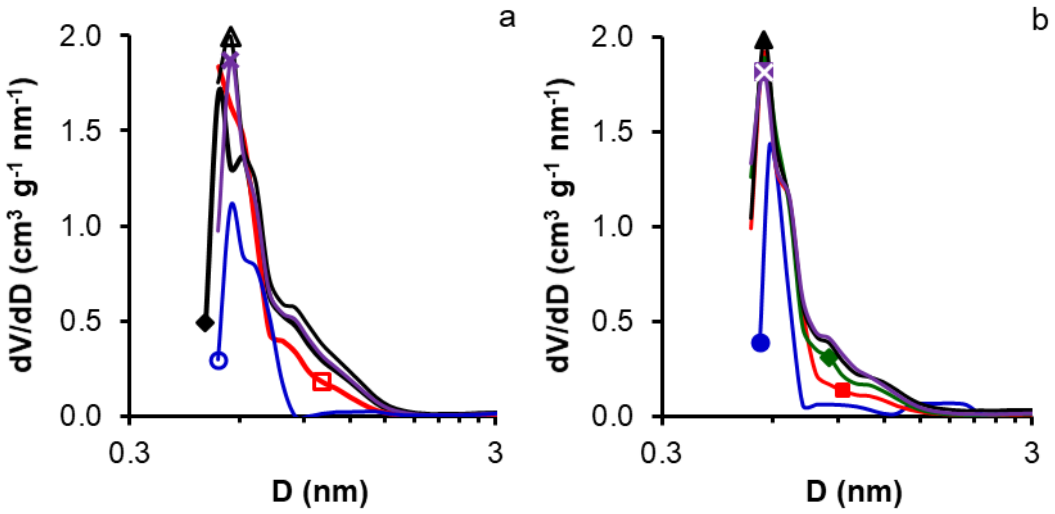

Figure 4. Pore size distribution obtained by applying the QSDFT method to N_2 isotherms at -196°C: (a) pristine and (b) N-doped carbon microspheres. Samples: S-0 and S-0-U (○), S-30 and S-30-U (□), S-60 and S-60-U (◇), S-90 and S-90-U (△), S-120 and S-120-U (×).

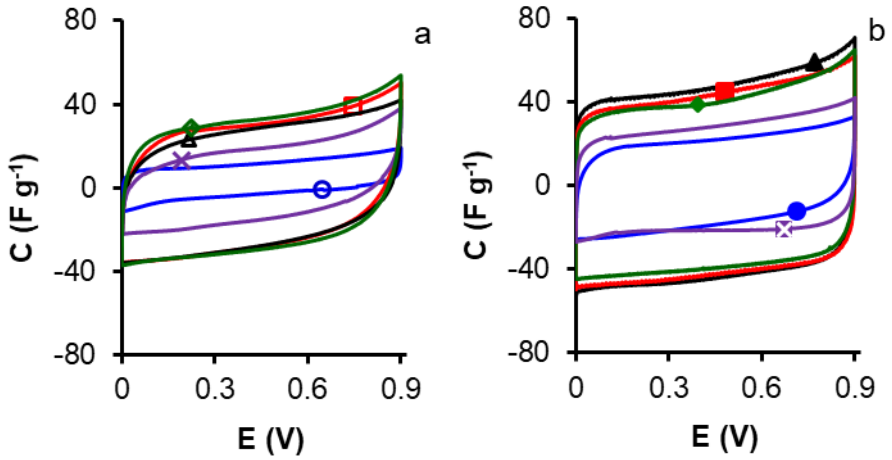

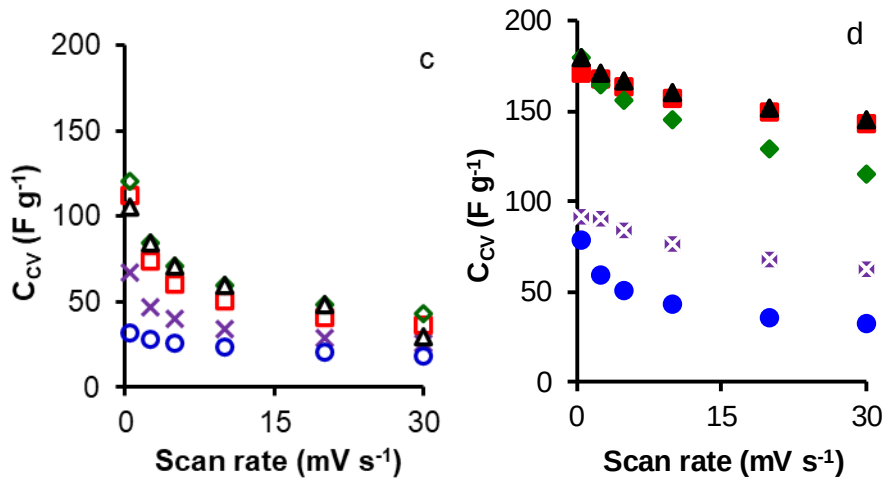

Figure 5. Cyclic voltamograms of: (a) CO_2-activated and (b) N-functionalized samples at a scan rate of 0.5 mV s^{-1}. Variation of the electrode capacitance as a function of scan rate for: (c) CO_2-activated and (d) N-doped carbon microspheres. Samples: S-0 and S-0-U (○), S-30 and S-30-U (□), S-60 and S-60-U (◇), S-90 and S-90-U (△), S-120 and S-120-U (×).

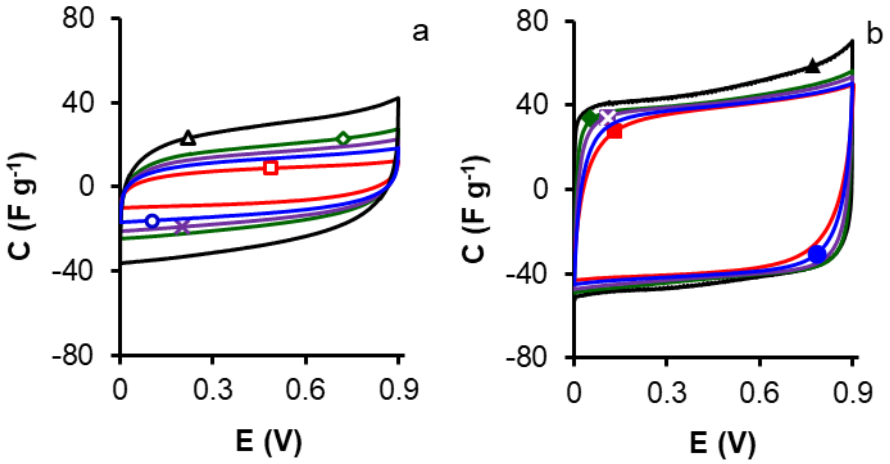

Figure 6. Cyclic voltamograms of: (a) CO_2-activated and (b) N-functionalized samples at different scan rates for samples (a) S-90 and (b) S-90-U. (△), 0.5; (◇), 5; (×), 10; (○), 20 and (□), 30 mV s^{-1}.

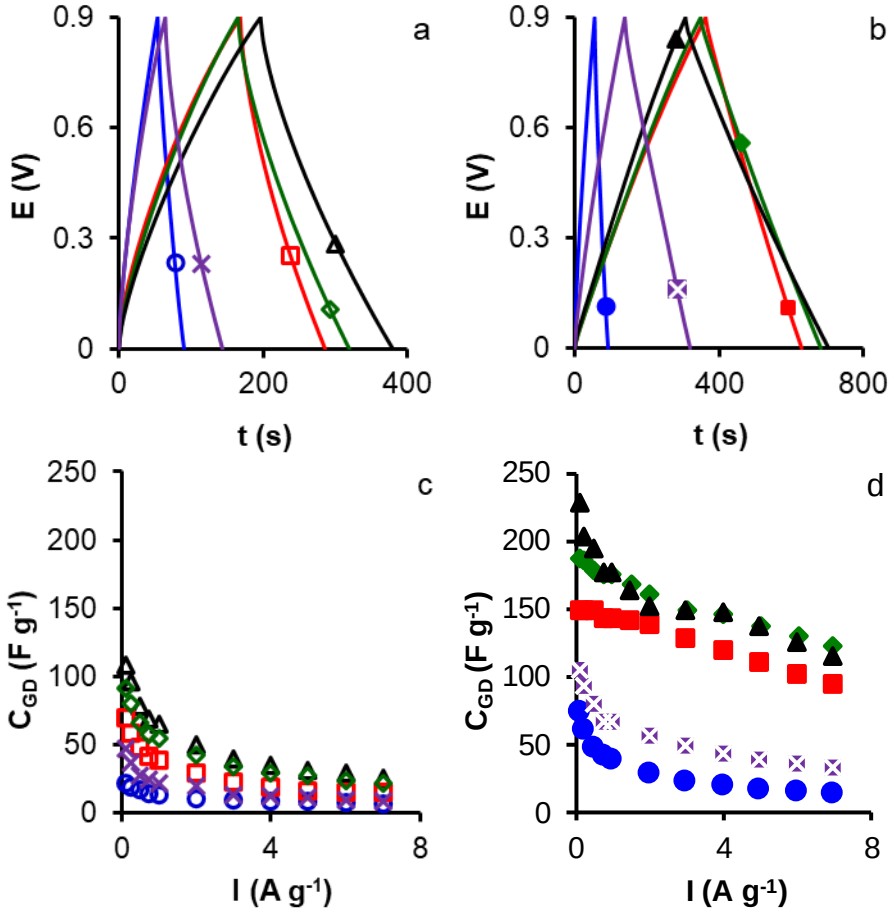

Figure 7. Galvanostatic charge-discharge curves of: (a) CO_2-activated and (b) N-doped carbon microspheres at a current density of 125 mA g^{-1}. Variation of the electrode capacitance with the current density for: (c) CO_2-activated and (d) N-functionalized samples. Samples: S-0 and S-0-U (○), S-30 and S-30-U (□), S-60 and S-60-U (◇), S-90 and S-90-U (△), S-120 and S-120-U (×).

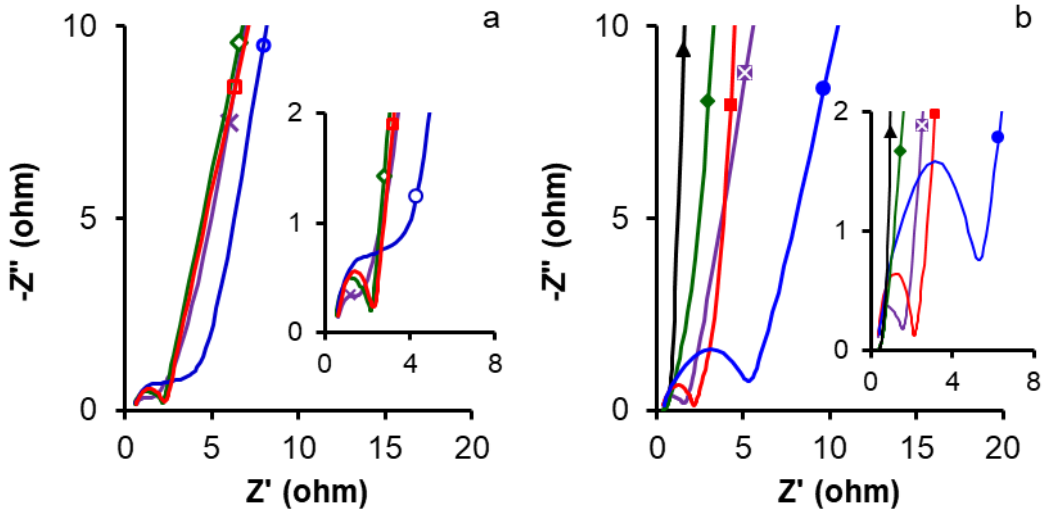

Figure 8. Nyquist plot of the electrodes based on: (a) CO_2-activated and (b) N-doped carbon microspheres. S-0 and S-0-U (○), S-30 and S-30-U (□), S-60 and S-60-U (◇), S-90 and S-90-U (△), S-120 and S-120-U (×).

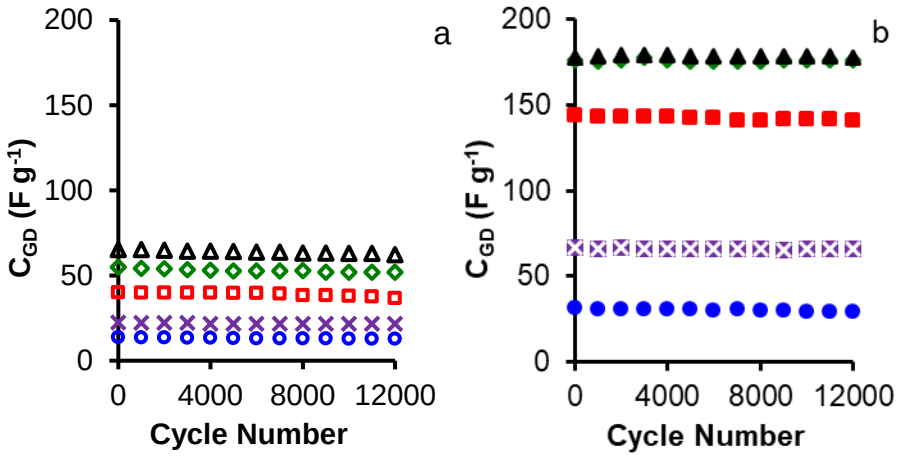

Figure 9. Variation of the gravimetric electrode capacitance (C_{GD}) with the number of charge-discharge cycles at a current density of 1 A g^{-1} in the potential window between 0 and 0.9 V for a) CO_2-activated and b) N-doped carbon microspheres. Samples: S-0 and S-0-U (○), S-30 and S-30-U (□), S-60 and S-60-U (◇), S-90 and S-90-U (△), S-120 and S-120-U (✖).

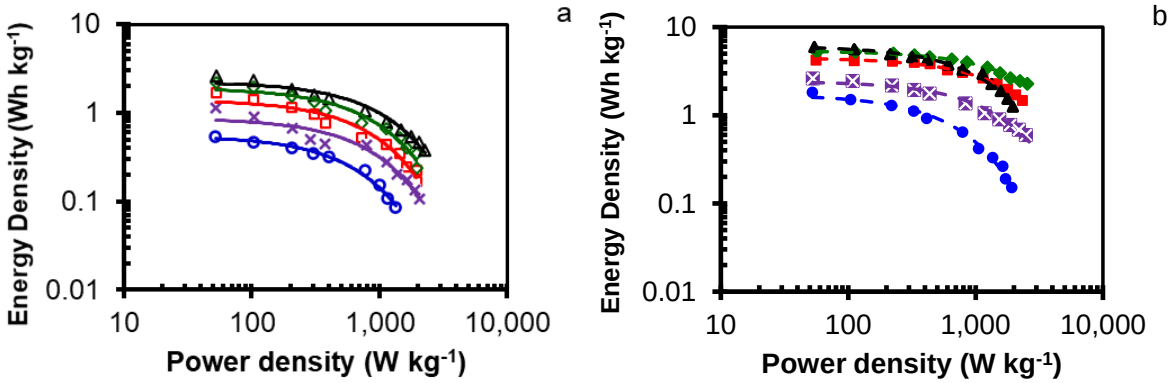

Figure 10. Ragone plots of all carbon microspheres in 1 mol L^{-1} H_2SO_4 for: (a) CO_2-activated and (b) N-functionalized carbons microspheres. Samples: S-0 and S-0-U (○), S-30 and S-30-U (□), S-60 and S-60-U (◇), S-90 and S-90-U (△), S-120 and S-120-U (×).

Table 1. BET area (A_{BET}), micropore volume (W_0), total pore volume ($V_{0.95}$), mesopore volume (V_{meso}) and average pore diameter (L_0) of the activated and doped samples.

Sample	N_2 at -196 ºC					CO_2 at 0 ºC	
	A_{BET}	L_0 (N_2)	W_0 (N_2)	$V_{0.95}$ (N_2)	V_{meso} (N_2)	L_0 (CO_2)	W_0 (CO_2)
	$m^2\ g^{-1}$	nm	$cm^3\ g^{-1}$	$cm^3\ g^{-1}$	$cm^3\ g^{-1}$	nm	$cm^3\ g^{-1}$
S-0	600	0.58	0.233	0.321	0.088	0.83	0.301
S-30	1158	0.73	0.461	0.553	0.092	0.72	0.409
S-60	1377	1.03	0.545	0.700	0.155	0.65	0.445
S-90	1513	0.95	0.602	0.753	0.151	0.65	0.440
S-120	1380	0.88	0.549	0.694	0.145	0.68	0.409
S-0-U	224	1.27	0.089	0.188	0.078	0.56	0.260
S-30-U	990	0.93	0.396	0.481	0.085	0.62	0.412
S-60-U	1195	0.75	0.473	0.578	0.106	0.66	0.460
S-90-U	1343	0.86	0.529	0.677	0.148	0.65	0.440
S-120-U	1236	0.85	0.491	0.617	0.126	0.68	0.408
S-90-2U	1322	0.87	0.501	0.601	0.140	0.66	0.414

Table 2. Elemental analysis (E.A.) and XPS of non-doped and N-doped carbon microspheres.

	E.A. (wt. %)			**XPS (wt. %)**			**N functionalities (%)**			**O-functionalities (%)**	
Sample	**C**	**N**	**O**	**C**	**N**	**O**	**N-6**	**N-5**	**N-Q**	**C=O**	**C-O**
S-0	93.2	0.3	5.5	97.1	-	2.9	-	-	-	47	53
S-30	94.0	0.4	5.1	-	-	-	-	-	-	-	-
S-60	92.5	0.5	6.5	-	-	-	-	-	-	-	-
S-90	93.9	0.5	5.1	-	-	-	-	-	-	-	-
S-120	93.9	0.4	5.2	-	-	-	-	-	-	-	-
S-0-U	89.5	4.5	4.5	93.5	4.0	2.5	50	40	10	45	55
S-30-U	89.3	4.4	5.4	94.3	3.6	2.1	49	38	13	50	50
S-60-U	88.9	4.4	5.6	94.1	3.6	2.3	50	40	10	45	55
S-90-U	90.0	3.8	5.4	94.7	3.2	2.1	49	40	11	45	55
S-120-U	90.8	2.9	5.7	94.4	3.1	2.5	50	37	13	45	55

S-90-2U	89.5	3.9	5.9	94.5	3.3	2.2	50	40	10	44	56

Table 3. C_{CV} at 0.5 mV s^{-1}; C_{GD} at 125 mA g^{-1}, R_2 and R_7: capacity retention at 2 and 7 A g^{-1} against 0.125 A g^{-1}, respectively and retention capacitance after 12000 charge-discharge cycles of GCD at 0.125 A g^{-1}**.**

Sample	C_{CV} F g^{-1}	C_{GD} F g^{-1}	R_2 %	R_7 %	CR_{12000} %
S-0	32	22	49	31	93
S-30	113	70	41	22	92
S-60	120	91	46	24	95
S-90	106	109	46	24	95
S-120	67	47	42	19	97
S-0-U	79	75	40	19	93
S-30-U	171	150	93	64	98
S-60-U	180	187	86	66	100
S-90-U	180	228	67	51	100
S-120-U	92	106	53	32	99

Table 4. Electrochemical capacitance performances of N-doped carbon and carbon spheres from the literature.

Sample type	**Name**	**N content (% wt.)**	**C_g (F g^{-1})**	**C_v (F g^{-1})**	**Density***	**Scan Rate**	**Electrolyte**	**Cell type**	**Ref.**
N-doped Carbon microspheres (CS)	S-60- U	4.4	187	159	Particle	0.125 A g^{-1}	1 M H_2SO_4	2EC	Our work
N-doped CS	S-90-U	3.8	228	199					
Carbon aerogel	B_a	-	110	42	Particle	0.35 A g^{-1}	1 M H_2SO_4	2EC	58
Carbon criogel	B_c	-	157	63					
Carbon xerogel	B_x	-	138	52					
Pomegranate-like N-doped CS	PCS	3.6	289	254	Electrode	1 A g^{-1}	6 M KOH	3EC	60
Monodisperse N-doped CS	CS	-	240	70					
N-doped carbon aerogel	CR4N	1.7	224	81	Particle	0.125 A g^{-1}	1 M H_2SO_4	3EC	33
N-doped carbon aerogel	CP4**N**	1.5	122	78					
N-doped 3D hierarchically porous carbon	NC-800	6.5	178	179	Electrode	0.5 A g^{-1}	1 M H_2SO_4	2EC	61
	NC-800		156	-			1 M KOH		
	NC-800		285	-			1 M KOH	3EC	

Lecithin-derived carbon	C-800	0.6	132	150			1 M H_2SO_4	2EC	
	C-800		130	-			1 M KOH		
	C-800		248	-			1 M KOH	3EC	
N, B-doped porous carbon-tube bundle electrodes	N-PCTBs	2.9	298	-	Electrode	1 A g^{-1}	6 M KOH	3EC	62
	B/N-PCTBs	2.2	355	27					
(O, N)-doped porous carbon	AC-700	2.1	29	8	Electrode	1 A g^{-1}	1 M H_2SO_4	2EC	63
	KAC-700	1.9	223	168					
	ZAC-700	4.2	188	121					
Nitrogen-Doped Carbon Aerogels	NAC-700	4.7	179	0.9**	Particle	0.5 A g^{-1}	1 M H_2SO_4	3EC	64
	NAC-800	4.3	300	1.5**					
	NAC-900	3.3	270	1.4**					
	NCA-1000	1.2	222	1.1**					
Hierarchical porous carbon materials	L-β-700	2.8	249	75	Particle	50 mA g^{-1}	1 M H_2SO_4	3EC	65
Monolithic Carbide-Derived Carbon Films	-	-	-	160	Electrode	-	1 M H_2SO_4	2EC	66
Reduced graphene oxide	RGO	-	255	196	Particle	0.5 A g^{-1}	6 M KOH	3EC	67
N,P,S-codoped hierarchically porous carbon spheres	N,P,S-HCS	6.7	274	219	Electrode	0.5 A g^{-1}	6 M KOH	3EC	16
N-doped microporous carbon microspheres	N-CSA-600	1.9	310	183	Particle	0.1 A g^{-1}	1 M H_2SO_4	2EC	68

*density used to calculate volumetric capacitances. ** calculated from manuscript data.

Table 5. Characterization obtained from EIS (ESR: equivalent series resistance and R_{CT}: interfacial charge transfer resistance) and Ragone plots (E_{max}: maximum energy density, E_{min}: minimum energy density, P_{max}: maximum power density and P_{min}: minimum power density)

Sample	ESR	R_{CT}	τ	E_{max}	E_{min}	P_{max}	P_{min}
	Ω	Ω	s	Wh kg^{-1}	Wh kg^{-1}	W kg^{-1}	W kg^{-1}
S-0	0.63	2.86	8.5	0.53	0.03	1208	52
S-30	0.60	1.74	8.8	1.69	0.17	1957	52
S-60	0.55	1.65	7.6	2.22	0.24	1957	52
S-90	N.D.	N.D.	N.D.	2.64	0.38	2269	52
S-120	0.65	0.85	7.2	1.14	0.11	2059	52
S-0-U	0.43	4.83	11.4	1.82	0.15	1919	52
S-30-U	0.38	1.81	1.1	4.20	1.47	2330	56
S-60-U	0.38	0.12	0.8	5.62	2.28	2548	43
S-90-U	0.36	0.08	0.3	5.94	1.25	1955	54

S-120-U	0.36	1.22	3.6	2.62	0.60	2482	53

Supplementary Materials

Gravimetric capacitances, C (F/g), were obtained from the cyclic voltammetry curves by Equation (1):[19,42]

$$C = \frac{\sum|I| \times \Delta t}{m \times \Delta V} \quad \text{(Eq. 1)}$$

where was the area of the current (A) against time (s) curve, Δt the discharge time, m the total mass of the carbon material in the electrodes, ΔV the voltage interval after the ohmic drop.

The gravimetric capacitance, C (F/g), was obtained from galvanostatic charge-discharge tests by equation 2:[43,44]

$$C = \frac{I_d \times \Delta t}{m \times \Delta V} \quad \text{(Eq. 2)}$$

where I_d is the discharge current, Δt the discharge time, m the total mass of the active material in the electrodes, and ΔV the voltage interval after the ohmic drop.

For performance comparisons, the gravimetric capacitances in two-electrodes configuration (2EC) were multiplied by four to obtain the expression per single electrode, (C_{CV} and C_{GD}, from cyclic voltammetry and galvanostatic charge-discharge tests, respectively) which is the 3-electrode configuration (3EC) equivalent.[69]

The electrical energy and the power density were calculated by using the Eq. 3 and Eq. 4, respectively for two-electrode cell:[45]

$$E(Wh\ kg^{-1}) = \frac{C\ (F\ g^{-1}) \times \Delta V^2\ (V)}{2 \times 3.6} \quad \text{(Eq. 3)}$$

$$P(W\ \text{kg}^{-1}) = \frac{E}{\Delta t} \quad \text{(Eq. 4)}$$

where ΔV is the operation voltage taken as $\Delta V = V_{max} - IR_{drop}$, Δt is the discharge time (h) and C are the values of the capacitances obtained from Eq. 2.

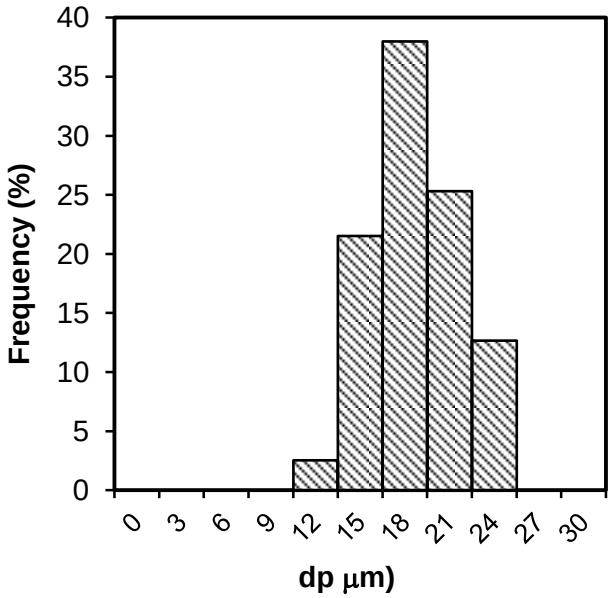

Figure S1. Particle size distribution of carbon microspheres obtained from the analysis of optical microscopy images.

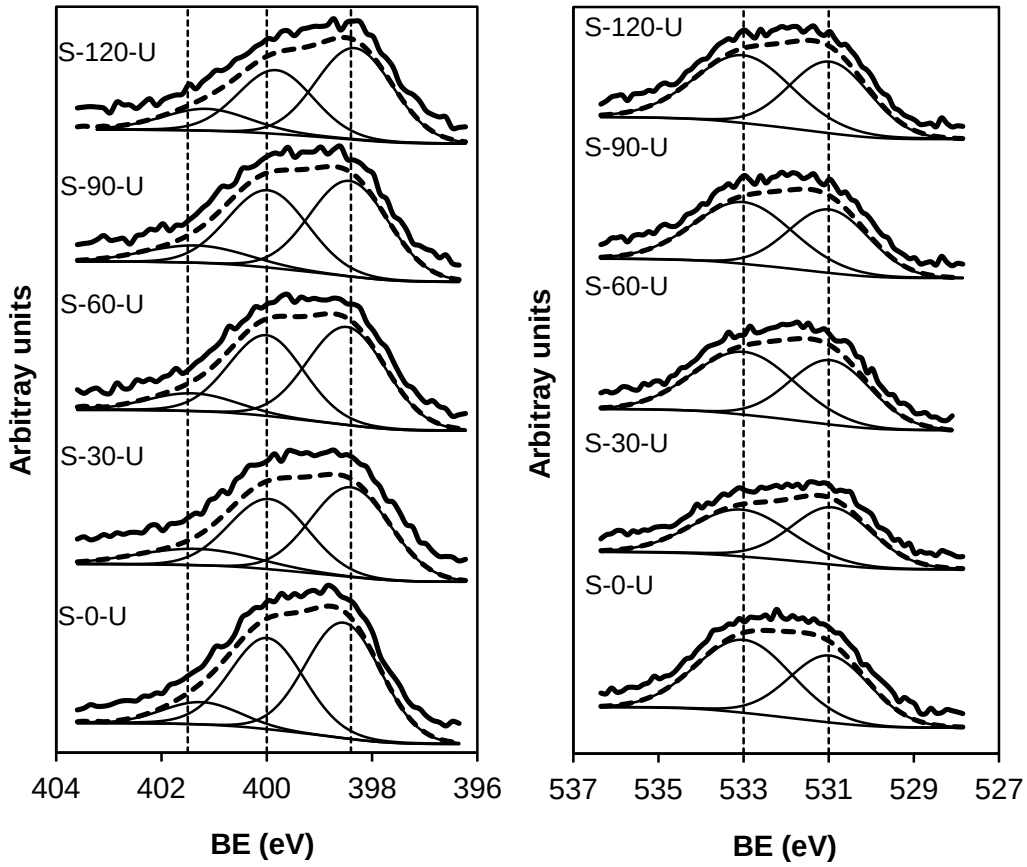

Figure S2. XPS spectra of urea-treated carbon microspheres: (a) N_{1s} and (b) O_{1s}